

SNM-Net: A Universal Framework for Robust Open-Set Gas Recognition via Spherical Normalization and Mahalanobis Distance

Shuai Chen^a, Chen Wang^a, Ziran Wang^{a, *}

^a School of Mechanical Engineering, Shandong University, Jinan 250061, China

Highlights

- A novel geometric framework that effectively eliminates signal drift in gas sensors
- Achieves 99.77% AUROC with near-zero variance across diverse operating conditions
- Architecture-agnostic design that enhances CNN, RNN, and Transformer backbones
- Mahalanobis distance captures anisotropic feature distributions
- Exceptional threshold stability significantly reduces industrial deployment complexity

Abstract

Electronic nose (E-nose) systems face two interconnected challenges in open-set gas recognition: feature distribution shift caused by signal drift and decision boundary failure induced by unknown gas interference. Existing methods predominantly rely on Euclidean distance or conventional classifiers to construct decision mechanisms, failing to adequately account for the anisotropic characteristics of gas feature distributions and the dynamic variations in signal intensity. To address these issues, this study proposes SNM-Net, a universal deep learning framework for open-set gas recognition. The core innovations of this framework lie in: achieving geometric decoupling through cascaded batch normalization and L2 normalization, projecting high-dimensional features onto a unit hypersphere to eliminate the influence of signal intensity fluctuations at the physical mechanism level; and introducing Mahalanobis distance as the core scoring mechanism, utilizing class-wise statistical information (mean vectors and covariance matrices) to construct adaptive ellipsoidal decision boundaries. SNM-Net exhibits remarkable architecture-agnostic properties and can be seamlessly integrated with mainstream backbone networks including CNN, RNN, and Transformer. Systematic experiments on the public Vergara dataset demonstrate that the Transformer+SNM configuration achieves near-

theoretical-limit performance, with an AUROC of 0.9977 ± 0.0028 and an unknown gas detection rate (TPR@FPR=5%) of 99.57%, significantly outperforming state-of-the-art methods (compared to CAC: +3.0% AUROC improvement, 91.0% standard deviation reduction). The framework maintains exceptional robustness across all five sensor positions, with standard deviations below 0.0028. This work effectively addresses the critical challenge of simultaneously achieving high accuracy and high stability in open-set gas recognition, providing solid theoretical and technical support for the industrial deployment of E-nose systems.

Keywords: Electronic nose; Open-set recognition; Spherical normalization; Mahalanobis distance; Gas sensor; Signal drift

1. Introduction

Electronic nose (E-nose) systems, as intelligent sensing technologies that emulate biological olfactory mechanisms, respond to gas mixtures through gas-sensitive sensor arrays and achieve automatic gas identification and concentration estimation through pattern recognition algorithms [1,2]. In recent years, this technology has demonstrated promising application prospects in food quality monitoring [3-6], medical diagnosis [7,8], industrial safety detection [9-11], and environmental monitoring [12,13]. With the rapid advancement of deep learning, researchers have proposed various neural network-based gas recognition methods, including convolutional neural networks [14-16], recurrent neural networks [17,18], and hybrid deep network architectures [19,20], which have achieved remarkable performance in closed-set recognition scenarios.

However, when extending E-nose systems from laboratory environments to practical industrial settings, a fundamental contradiction emerges between the closed-set assumption and open-world conditions. Traditional gas recognition methods adopt the closed-set assumption, wherein test samples must belong to one of the known classes defined during training. Nevertheless, the gas composition in real industrial environments is complex and variable. Metal oxide semiconductor (MOS) sensors exhibit high sensitivity to non-target odor interference in the environment, such as perfume, alcohol, and fruit aromas [21]. These background odors interfere with normal sensor responses, leading to misidentification of target gases and biased concentration estimates. In practical applications, there exist thousands of unknown "non-target" interference sources, and effectively

counteracting these unknown interferences has become a critical challenge for the practical deployment of E-nose technology [22,23].

Open-set recognition (OSR) provides an effective approach to address the aforementioned problems. Unlike closed-set recognition, OSR requires models not only to accurately classify known classes encountered during training but also to detect and reject unknown samples that were never present during training [24,25]. Scheirer et al. [26] first systematically defined the open-set recognition problem and proposed a solution based on the 1-vs-Set machine. Subsequently, Bendale and Boulton [27] proposed the OpenMax method, which models the activation vector distribution at class boundaries through extreme value theory, achieving open-set extension of deep neural networks. Rudd et al. [28] further developed the Extreme Value Machine (EVM), utilizing Weibull distributions to model sample inclusion probabilities. More recently, Miller et al. [29] proposed the Class Anchor Clustering (CAC) method, which enhances intra-class feature compactness through anchor constraint loss, achieving excellent performance on multiple benchmark datasets. Qu et al. [30] first applied open-set recognition methods to E-nose datasets, validating the effectiveness of the CAC-CNN method in gas open-set recognition tasks, achieving an average AUROC of 0.956. Building upon this, Ma et al. [31] proposed a multi-scale temporal convolutional network integrated with an SE-ResNet channel attention mechanism (MSE-TCN) for the open-set gas classification task in electronic noses, achieving a mean AUROC of 0.9657.

Despite the significant progress achieved by the aforementioned methods in the field of open-set recognition, two fundamental challenges remain when applying them to gas recognition tasks. A key limitation arises from the predominant use of Euclidean distance in existing open-set methods to construct decision boundaries, which implicitly assumes isotropic distribution in the feature space. However, the response characteristics of gas-sensitive sensor arrays exhibit significant anisotropic properties: different sensor channels show vastly different sensitivities to different gases. For instance, the TGS2611 sensor is sensitive to methane while the TGS2602 sensor is sensitive to ammonia [32]. Moreover, due to the physical proximity of sensors, non-trivial correlations exist among channels [33,34]. Consequently, the spherical decision boundaries corresponding to Euclidean distance cannot effectively adapt to such complex feature geometry, resulting in systematic deviations between boundaries and the true data manifold.

Further complicating this scenario is the issue of signal drift, which severely constrains the practical deployment capability of gas recognition systems. The response characteristics of gas-sensitive sensors are influenced by multiple factors, including dynamic fluctuations in gas concentration, variations in environmental temperature and humidity, sensor aging and poisoning effects, and spatial relationships between sensors and gas sources [35-37]. Zhang and Zhang [38] pointed out that sensor drift has been a long-standing challenge in the E-nose field; gas samples collected by drifted sensors exhibit different distribution characteristics compared to drift-free data, making classification tasks more difficult. Multiple studies [39-42] have been devoted to developing drift compensation methods, including transfer learning, domain adaptation, and ensemble learning strategies. However, these methods typically require labeled data from the target domain or complex online update mechanisms. More critically, signal drift not only affects the recognition accuracy of known classes but also interferes with threshold settings for unknown detection—thresholds trained under one condition may completely fail under other conditions, posing severe challenges for the practical deployment of traditional open-set methods.

Furthermore, feature vectors output by existing feature extraction methods simultaneously encode both chemical property information (directional component) and signal intensity information (magnitude component) of gases, lacking effective mechanisms to decouple these two types of information [43,44]. When signal drift occurs, the magnitude of feature vectors changes; even if their direction remains stable, distance-based classifiers will produce erroneous judgments. Existing methods fail to fundamentally address this issue, making it difficult for models to distinguish between genuine chemical differences and intensity variations caused by concentration fluctuations or equipment aging.

Figure 1 illustrates the signal drift optimization process and provides an intuitive schematic of the open-set gas recognition problem. In the feature space, effective decision boundaries need to be established between known and unknown classes, while signal drift causes the feature distribution of the same gas to shift under different conditions, making originally clear decision boundaries blurred or ineffective.

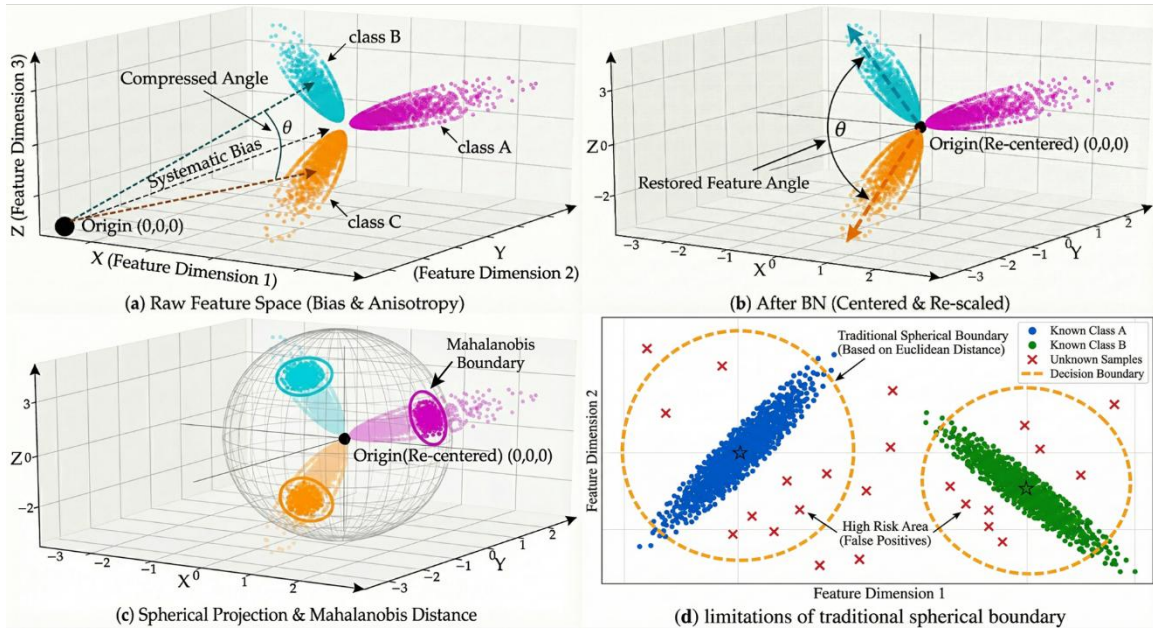


Figure 1. Schematic diagram of signal drift optimization and open-set gas recognition problem. (a) Original feature space (bias and anisotropy) (b) Features after BN (centering and rescaling) (c) Features after spherical projection and Mahalanobis distance (d) Limitations of traditional spherical boundary

To address the aforementioned problems, this study proposes SNM-Net (Spherical Normalization and Mahalanobis Distance Network)—a universal deep learning framework for open-set gas recognition. The core innovations of this framework encompass three aspects:

(1) A geometric decoupling mechanism based on spherical manifold projection is proposed, which projects deep features onto a unit hypersphere through cascaded batch normalization and L2 normalization, mathematically achieving complete decoupling of direction and magnitude of feature vectors, enabling model decisions to rely solely on directional information, thereby eliminating interference from signal intensity fluctuations at the physical root;

(2) Mahalanobis distance is introduced as the core scoring mechanism, modeling correlations among feature dimensions through covariance matrices and constructing adaptive ellipsoidal decision boundaries to achieve conformal adaptation between decision boundaries and the true data manifold;

(3) An architecture-agnostic post-processing module is designed that can be seamlessly embedded into mainstream backbone networks such as CNN, RNN, and Transformer, elevating the open-set recognition performance of various architectures to near-theoretical limits.

2. Materials and Methods

2.1 Dataset Description

This study employed the publicly available gas sensor dataset released by Vergara et al. for experimental validation. This dataset enjoys widespread recognition in the gas recognition field and has been used to evaluate the performance of various recognition algorithms. Data collection was conducted in a wind tunnel environment, yielding 18,000 time-series gas samples covering ten high-priority chemical gaseous substances: acetone, acetaldehyde, ammonia, butanol, ethylene, methane, methanol, carbon monoxide, benzene, and toluene.

The experimental system utilized nine identical metal oxide gas sensor modules, each containing eight different commercial sensors (TGS series), totaling 72 sensing elements. Table 1 provides detailed specifications of each sensor model and their target detection gases. This redundant design enhances system robustness against sensor noise and failures while providing rich multidimensional feature information. Release concentrations for each gas were set according to their physicochemical properties and practical application scenarios, with source concentrations ranging from 100 ppmv (butanol) to 10,000 ppmv (ammonia).

Data acquisition for each sample lasted 260 seconds, during which sensor resistance values were recorded at a frequency of 100 Hz. To systematically evaluate the impact of signal drift on recognition performance, data collection was conducted at six different positions (L1-L6), with distances between the sensor array and gas release source incrementally increasing from 1 to 4 meters. As distance increases, gas concentration decays exponentially, resulting in significantly reduced sensor response intensity. This study utilized data from positions L1-L5, excluding position L6 to ensure the signal-to-noise ratio met analysis requirements. Each sub-dataset contains 300 samples per gas class.

Raw sensor response sequences underwent the following preprocessing steps: First, temporal downsampling was performed by computing the average of 100 sampling points per second, reducing

the sampling frequency to 1 Hz and thereby regularizing the response sequence to 260 time steps; subsequently, z-score normalization was applied channel-wise to eliminate baseline differences among different sensors; finally, the processed data was restructured into a 260×72 two-dimensional spatiotemporal feature map, where 260 represents the temporal dimension and 72 represents the spatial channel dimension.

Table 1. Sensor configuration of the Vergara gas sensing dataset

Sensor Model	Quantity per Array	Target Gases (Manufacturer Specifications)
TGS2600	1	Hydrogen, Carbon monoxide
TGS2602	2	Ammonia, Hydrogen sulfide, VOCs
TGS2610	1	Propane
TGS2611	1	Methane
TGS2612	1	Methane, Propane, Butane
TGS2620	2	Carbon monoxide, Combustible gases, VOCs
Total	8	(9 modules × 8 sensors = 72 sensors)

2.2 Experimental Protocol

This study employed a 10-fold cross-validation strategy to evaluate model performance. For each sub-dataset, the ten gas types were randomly partitioned into six known classes and four unknown classes. Sixty percent of samples from known classes were randomly selected as the training set (1,080 samples in total), while samples from unknown classes were excluded from training. The test set comprised 40% of randomly selected samples from unknown classes combined with remaining samples from known classes (1,200 samples in total). This random partitioning process was repeated 10 times to evaluate each model.

To comprehensively assess model performance under different conditions, this study designed 50 independent experiments (5 positions × 10 folds). Each experiment conducted a complete training-validation-testing procedure on a specific position and fold partition, with final results reported as statistical summaries across all experiments (mean ± standard deviation). This design ensures both evaluation comprehensiveness and adequate sample size for statistical significance analysis.

This study employed three complementary metrics for comprehensive model performance evaluation. Known Class Accuracy measures the model's classification capability for known gas classes, calculated as the proportion of correctly classified samples among known class test samples. True Positive Rate at Fixed False Positive Rate (TPR@FPR=5%) measures the model's capability to detect unknown gases under a constraint of 5% false positive rate, directly reflecting detection efficacy in practical deployment scenarios. Area Under the ROC Curve (AUROC) comprehensively measures unknown detection performance across all possible thresholds and serves as the core evaluation metric for open-set recognition. Given the limited number of classes in this dataset, partitioning an independent validation set for threshold optimization proves impractical; therefore, AUROC was adopted as the primary evaluation metric, as it requires no predetermined threshold and is more suitable for performance evaluation in open-set gas recognition.

2.3 SNM-Net Framework Architecture

The overall architecture of the SNM-Net framework adopts a modular design, comprising five core components: an input data processing module, a feature extractor (backbone network), a geometric refinement module, a statistical scoring module, and a decision layer. The input two-dimensional feature map undergoes high-level semantic feature extraction through the backbone network, followed by projection onto the unit hypersphere through the geometric refinement module, and finally open-set decisions are made by the statistical scoring module based on Mahalanobis distance calculations. Figure 2 illustrates the overall architecture of the SNM-Net framework.

SNM-Net: Spherical Normalization and Mahalanobis Distance Framework

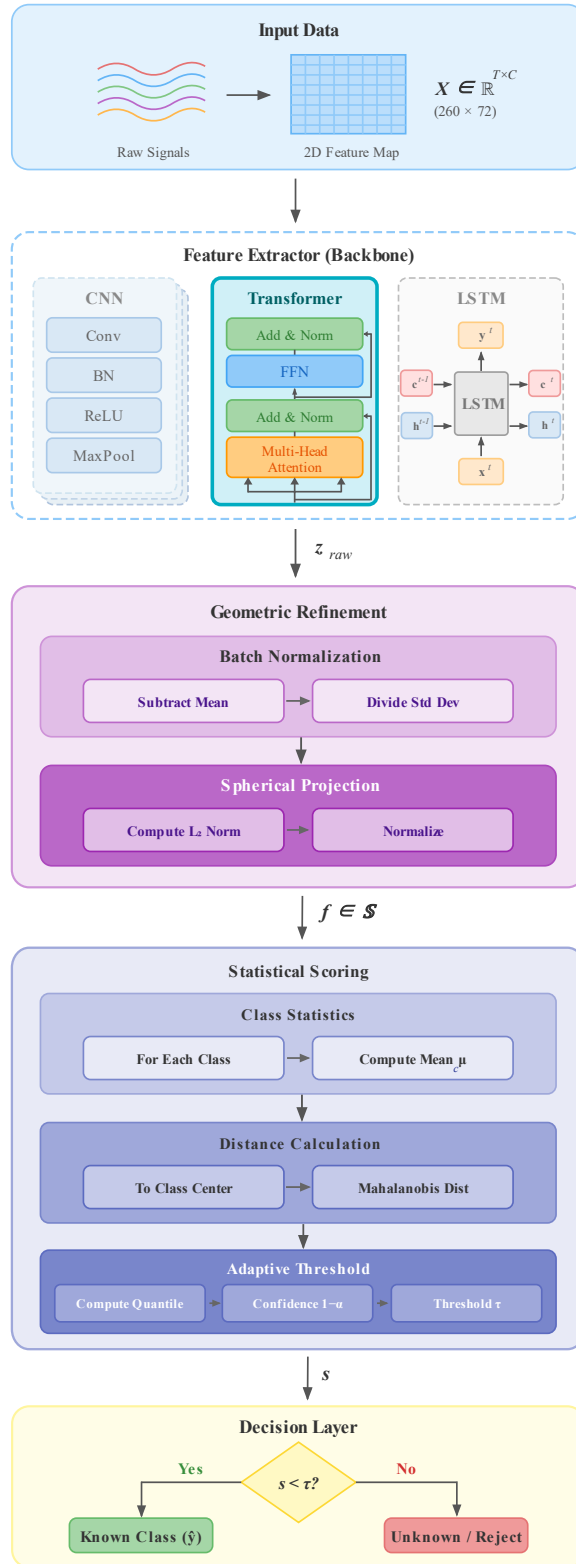


Figure 2. Overall architecture diagram of the SNM-Net framework.

2.3.1 Backbone Network Design

The SNM-Net framework possesses architecture-agnostic properties and supports multiple types of feature extraction backbone networks. This study implemented and compared three representative architectures.

The Transformer encoder serves as the primary configuration in this study, effectively capturing long-range dependencies in spatiotemporal sequences through self-attention mechanisms. Let the input feature map be $\mathbf{X} \in \mathbb{R}^{T \times C}$, where $T = 260$ denotes the number of time steps and $C = 72$ denotes the number of channels. The input is first mapped to the model dimension through linear projection:

$$\mathbf{H}^{(0)} = \mathbf{X}\mathbf{W}_{\text{proj}} + \mathbf{E}_{\text{pos}}$$

where $\mathbf{W}_{\text{proj}} \in \mathbb{R}^{C \times d_{\text{model}}}$ is the projection matrix, $d_{\text{model}} = 128$ is the model dimension, and $\mathbf{E}_{\text{pos}} \in \mathbb{R}^{T \times d_{\text{model}}}$ represents learnable positional encodings.

The Transformer encoder consists of $L = 2$ stacked layers, each containing a multi-head self-attention sublayer and a feed-forward network sublayer. The multi-head attention mechanism is defined as:

$$\text{MultiHead}(\mathbf{H}) = \text{Concat}(\text{head}_1, \dots, \text{head}_h)\mathbf{W}^O$$

$$\text{head}_i = \text{Attention}(\mathbf{H}\mathbf{W}_i^Q, \mathbf{H}\mathbf{W}_i^K, \mathbf{H}\mathbf{W}_i^V)$$

This study sets the number of attention heads to $h = 4$. Finally, temporal information is aggregated through global average pooling to obtain a fixed-length feature vector $\mathbf{z}_{\text{raw}} \in \mathbb{R}^d$.

For comparison, this study also implemented a CNN backbone network and a bidirectional LSTM backbone network. The CNN alleviates gradient vanishing problems in deep networks through residual connections and is suitable for extracting spatially hierarchical features; the LSTM selectively retains or forgets historical information through gating mechanisms, effectively handling long-sequence dependency problems.

2.3.2 Geometric Refinement Module

The geometric refinement module represents one of the core innovations of SNM-Net. Through cascaded batch normalization and L2 normalization, it projects raw features onto the unit hypersphere, achieving decoupling of feature direction and magnitude.

Let the raw features output by the backbone network be $\mathbf{z}_{\text{raw}} \in \mathbb{R}^d$. The batch normalization operation is defined as:

$$\hat{\mathbf{z}} = \frac{\mathbf{z}_{\text{raw}} - \boldsymbol{\mu}_B}{\sqrt{\boldsymbol{\sigma}_B^2 + \epsilon}}$$

where $\boldsymbol{\mu}_B$ and $\boldsymbol{\sigma}_B^2$ are the mean and variance vectors of the current batch, respectively, and ϵ is a numerical stability constant. Batch normalization eliminates distributional shift and scale differences in features, providing standardized distributions with approximately zero mean and unit variance, establishing stable input for subsequent spherical projection.

L2 normalization is then applied to batch-normalized features, projecting them onto the unit hypersphere \mathbb{S}^{d-1} :

$$\mathbf{f} = \frac{\hat{\mathbf{z}}}{\|\hat{\mathbf{z}}\|_2}$$

where $\|\cdot\|_2$ denotes the Euclidean norm. The projected features \mathbf{f} satisfy the constraint $\|\mathbf{f}\|_2 = 1$, meaning all feature vectors reside on the $(d - 1)$ -dimensional unit hypersphere. This geometric refinement process carries clear physical significance: raw feature vectors can be decomposed into a directional component (unit vector \mathbf{f}) and a magnitude component (scalar $\|\mathbf{z}_{\text{raw}}\|_2$). In gas recognition tasks, the directional component primarily encodes chemical property information of gases, while the magnitude component primarily reflects signal intensity information. Through spherical projection, model decisions are based entirely on directional information, fundamentally eliminating interference from signal intensity fluctuations.

Figures 3(a-b) demonstrate the effects of geometric refinement. Raw feature magnitudes exhibit significant differences across sensor positions, whereas after geometric refinement, feature

magnitudes from all positions are uniformly normalized to 1.0, achieving cross-position geometric alignment.

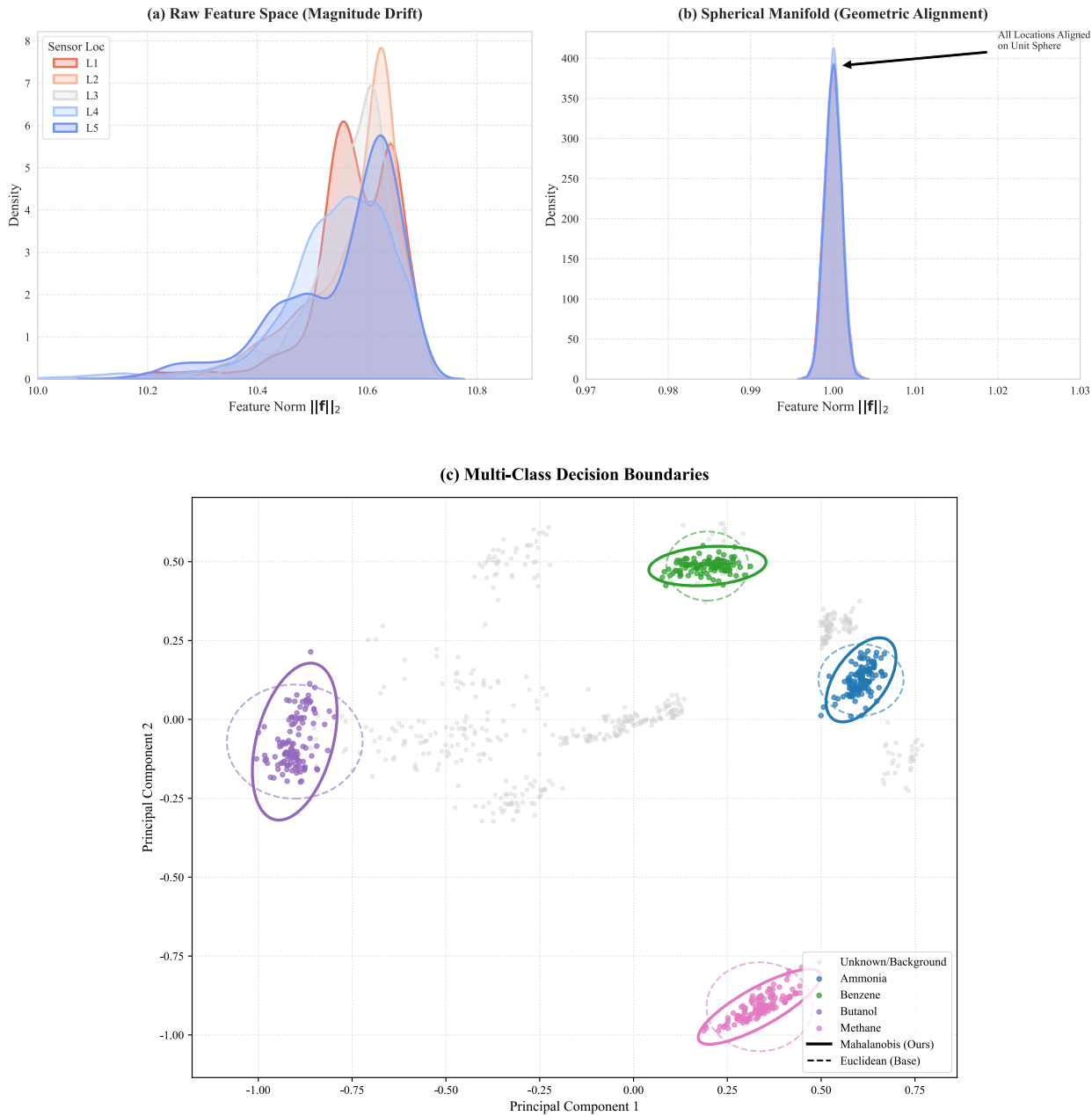


Figure 3. Schematic diagram of core principles. (a) Feature magnitude distribution across different positions (L1-L5) in the original feature space (b) Features after spherical normalization with all positions aligned (c) Comparison of Mahalanobis distance (solid ellipse) and Euclidean distance (dashed circle) decision boundaries

2.3.3 Statistical Scoring Module

The statistical scoring module computes confidence scores for sample membership in each known class based on Mahalanobis distance and makes open-set decisions accordingly. During training, statistics are computed for each known class $c \in \{1, 2, \dots, K\}$:

$$\boldsymbol{\mu}_c = \frac{1}{N_c} \sum_{i:y_i=c} \mathbf{f}_i$$
$$\boldsymbol{\Sigma}_c = \frac{1}{N_c - 1} \sum_{i:y_i=c} (\mathbf{f}_i - \boldsymbol{\mu}_c) (\mathbf{f}_i - \boldsymbol{\mu}_c)^\top$$

where $\boldsymbol{\mu}_c \in \mathbb{R}^d$ is the mean vector (class center) of class c , $\boldsymbol{\Sigma}_c \in \mathbb{R}^{d \times d}$ is the covariance matrix of class c , and N_c is the number of samples in class c . To improve numerical stability and prevent covariance matrix singularity, a regularization term is introduced:

$$\tilde{\boldsymbol{\Sigma}}_c = \boldsymbol{\Sigma}_c + \lambda \mathbf{I}$$

where $\lambda = 10^{-4}$ is the regularization coefficient and \mathbf{I} is the identity matrix.

For a test sample \mathbf{x} , the Mahalanobis distance from its spherical feature $\mathbf{f}(\mathbf{x})$ to each class center is computed:

$$D_M(\mathbf{f}(\mathbf{x}), c) = \sqrt{(\mathbf{f}(\mathbf{x}) - \boldsymbol{\mu}_c)^\top \tilde{\boldsymbol{\Sigma}}_c^{-1} (\mathbf{f}(\mathbf{x}) - \boldsymbol{\mu}_c)}$$

The fundamental advantage of Mahalanobis distance over Euclidean distance lies in: automatically weighting different feature dimensions through the inverse covariance matrix $\tilde{\boldsymbol{\Sigma}}_c^{-1}$ while accounting for inter-dimensional correlations. As illustrated in Figure 3(c), this results in ellipsoidal decision boundaries that adaptively conform to the anisotropic geometric structure of data distributions. In practical computation, Cholesky decomposition is employed to enhance numerical stability and computational efficiency.

The rejection score for sample \mathbf{x} is defined as its Mahalanobis distance to the nearest class center:

$$s(\mathbf{x}) = \min_{c \in \{1, \dots, K\}} D_M(\mathbf{f}(\mathbf{x}), c)$$

The predicted class is the one with the minimum distance:

$$\hat{y}(\mathbf{x}) = \operatorname{argmin}_{c \in \{1, \dots, K\}} D_M(\mathbf{f}(\mathbf{x}), c)$$

The final decision rule is:

$$\text{Output} = \begin{cases} \hat{y}(\mathbf{x}) & \text{if } s(\mathbf{x}) < \tau \\ \text{Unknown (Reject)} & \text{if } s(\mathbf{x}) \geq \tau \end{cases}$$

where τ is the rejection threshold, adaptively determined based on the 95th percentile of the score distribution on the validation set.

2.4 Training Strategy and Hyperparameters

Table 2 provides detailed hyperparameter configurations for model training. This study employs the CAC loss function for training, which simultaneously optimizes classification performance and intra-class feature compactness:

$$\mathcal{L} = \mathcal{L}_{\text{CE}} + \lambda_{\text{anchor}} \mathcal{L}_{\text{anchor}}$$

where \mathcal{L}_{CE} is the cross-entropy loss, $\mathcal{L}_{\text{anchor}}$ is the anchor constraint loss, and $\lambda_{\text{anchor}} = 10^{-5}$ is the balancing coefficient. The Adam optimizer is employed with an initial learning rate of 4×10^{-5} and a weight decay coefficient of 10^{-4} . Training incorporates an early stopping mechanism: training terminates when validation loss fails to decrease for 10 consecutive epochs, and model parameters with optimal validation performance are saved.

Table 2. Model hyperparameter configuration

Parameter	Value	Description
Optimizer	Adam	Model parameter update optimizer
Batch size	16	Samples per gradient descent iteration
Learning rate	4×10^{-5}	Initial optimizer learning rate
Weight decay	1×10^{-4}	L2 regularization coefficient
Max epochs	25	Maximum training iterations
Early stopping patience	10	Tolerance epochs without validation loss decrease
Random seed	41	Ensures experimental reproducibility
Dropout rate	0.1	Random neuron deactivation ratio
λ (CAC loss)	1×10^{-5}	Anchor constraint term weight
Covariance regularization	1×10^{-4}	Ensures covariance matrix positive definiteness

2.5 Baseline Methods and Comparison Models

To comprehensively evaluate the performance of SNM-Net, this study implemented the following comparison methods. The Softmax baseline trains a classifier using standard cross-entropy loss and uses the negative maximum softmax probability as the rejection score, representing the direct application of traditional closed-set classifiers to open-set scenarios. EVM constructs decision boundaries based on extreme value theory, modeling class boundaries through Weibull distributions, and represents a classical open-set recognition method. CAC introduces the class anchor concept and enhances intra-class feature compactness through anchor constraint loss, using Euclidean distance as the scoring mechanism, and represents a state-of-the-art method in the open-set recognition field. To ensure fair comparison, all comparison methods utilize identical backbone network architectures, training data partitions, and hyperparameter configurations.

3. Results

3.1 Ablation Study: Verification of Individual Module Contributions

To systematically validate the individual contributions and synergistic effects of each SNM-Net component, this section conducts ablation experiments using the CNN backbone network. CNN was selected as the backbone for ablation experiments because its moderate baseline performance clearly demonstrates the gain contributed by each module. Table 3 presents quantitative results of the

ablation experiments, where the baseline configuration (BASE-CNN) uses only CAC loss and Euclidean distance scoring as the control group.

Table 3. Quantitative results of ablation experiments (CNN backbone network)

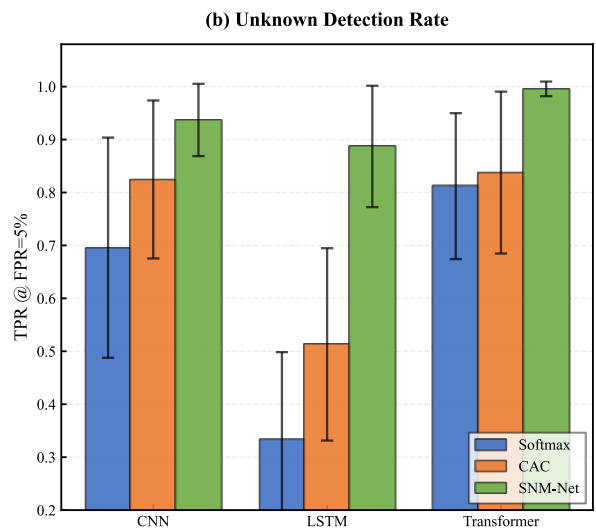
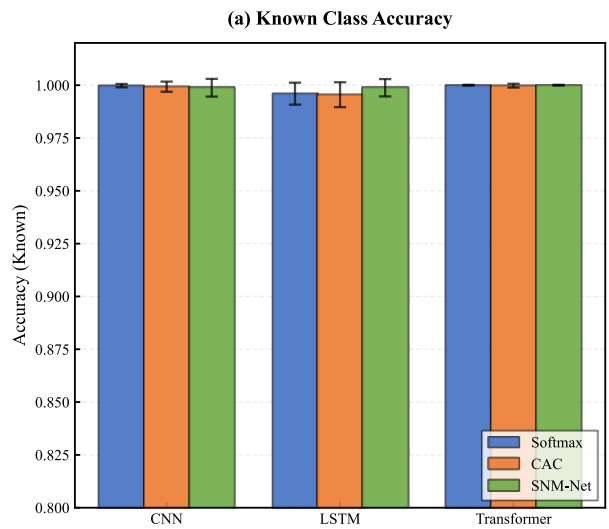
Configuration	Accuracy (Known)	TPR (Unknown)	AUROC
BASE-CNN (CAC only)	0.9993±0.0024	0.8246±0.1492	0.9504±0.0474
CNN+M	0.9974±0.0062	0.9045±0.0837	0.9785±0.0192
CNN+M+BN	0.9991±0.0026	0.9347±0.0732	0.9847±0.0169
CNN+M+L2N	0.9986±0.0052	0.9270±0.0811	0.9829±0.0168
CNN+M+BN+L2N (Full)	0.9988±0.0042	0.9370±0.0683	0.9846±0.0148

Comparing BASE-CNN with CNN+M configurations reveals that introducing Mahalanobis distance improved AUROC from 0.9504 to 0.9785, an absolute improvement of 2.81 percentage points; TPR improved from 82.46% to 90.45%, an absolute improvement of 7.99 percentage points. Simultaneously, the standard deviation of AUROC decreased from 0.0474 to 0.0192, a reduction of 59.5%. These results demonstrate that Mahalanobis distance effectively captures the anisotropic distribution of features through covariance modeling, significantly enhancing both the accuracy and stability of unknown detection.

Further comparison between CNN+M and CNN+M+BN configurations shows that introducing batch normalization improved AUROC to 0.9847, TPR to 93.47%, and reduced standard deviation from 0.0192 to 0.0169, indicating that batch normalization enhances cross-condition model consistency by stabilizing feature distributions. Similarly, L2 normalization also yields significant improvements: AUROC increased from 0.9785 to 0.9829, and standard deviation decreased from 0.0192 to 0.0168, validating the effectiveness of spherical projection in eliminating intensity information. The full configuration (CNN+M+BN+L2N) achieves the lowest standard deviation (0.0148), demonstrating that the cascade of BN and L2N indeed enhances model robustness. Compared to the baseline, AUROC improved by 3.42 percentage points and standard deviation decreased by 68.8%.

3.2 Cross-Architecture Generalization Verification

To verify the architecture-agnostic properties of the SNM-Net framework, this section conducts systematic comparative experiments across three representative backbone networks: CNN, LSTM, and Transformer. Figure 4 presents grouped bar charts comparing cross-architecture performance.



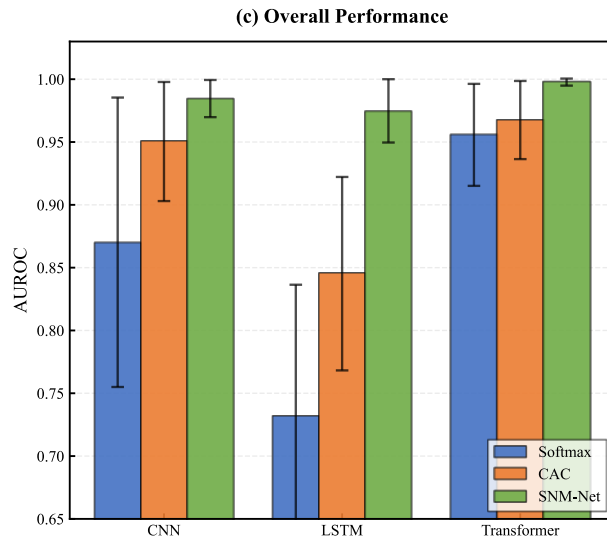


Figure 4. Grouped bar charts of cross-architecture performance comparison. (a) Known class classification accuracy (b) Unknown detection rate (TPR@FPR=5%) (c) Overall performance (AUROC)

For known class classification tasks, all three methods perform excellently, with accuracy generally exceeding 99.7%, indicating that the introduction of open-set mechanisms does not compromise the model's discriminative capability for known classes. Unknown detection rate serves as the key metric differentiating method performance: SNM-Net achieves significant improvements across all architectures. On the CNN backbone, SNM-Net improves over CAC by 11.24 percentage points; on the LSTM backbone by 50.40 percentage points; and on the Transformer backbone by 15.81 percentage points. Even on the less expressive LSTM backbone, SNM-Net still achieves a 95.57% unknown detection rate.

The AUROC metric comprehensively reflects model performance across all possible thresholds. SNM-Net achieves AUROC > 0.97 across all three architectures: CNN+SNM at 0.9846 ± 0.0148 , LSTM+SNM at 0.9748 ± 0.0198 , and Transformer+SNM at 0.9977 ± 0.0028 . Experimental results demonstrate that SNM-Net provides greater absolute improvements for weaker backbones while pushing stronger backbones toward near-theoretical limits.

3.3 Comprehensive Comparison with State-of-the-Art Methods

Table 4 presents a comprehensive performance comparison between SNM-Net and various open-set recognition methods using the Transformer backbone network.

Table 4. Comprehensive performance comparison with state-of-the-art methods (Transformer backbone network)

Method	Accuracy (Known)	TPR (Unknown)	AUROC
Softmax + Transformer	1.0000±0.0002	0.8120±0.1378	0.9557±0.0406
EVM + Transformer	0.9999±0.0004	0.8227±0.1339	0.9514±0.0424
CAC + Transformer	0.9998±0.0009	0.8376±0.1529	0.9675±0.0311
SNM + Transformer	1.0000±0.0002	0.9957±0.0138	0.9977±0.0028
Literature Methods			
Qu et al. (2022) CAC+CNN	0.9999	-	0.9560±0.0220
Ma et al. (2024) MSE-TCN	0.9999	-	0.9657

Compared to the Softmax baseline, SNM-Net improves AUROC by 4.20 percentage points, TPR by 18.37 percentage points, and reduces standard deviation from 0.0406 to 0.0028, a decrease of 93.1%. Compared to CAC, SNM-Net improves AUROC by 3.02 percentage points, TPR by 15.81 percentage points, and reduces standard deviation by 91.0%. This significant improvement is attributed to two factors: SNM-Net's geometric refinement module eliminates intensity drift that CAC cannot handle, and Mahalanobis distance more accurately describes anisotropic feature distributions compared to CAC's Euclidean distance. Figure 5 presents ROC curve comparisons among major methods, where the Transformer-SNM curve (red solid line) is closest to the upper-left corner with an AUC of 0.9977, significantly outperforming Transformer-CAC, LSTM-SNM, and Transformer-Softmax.

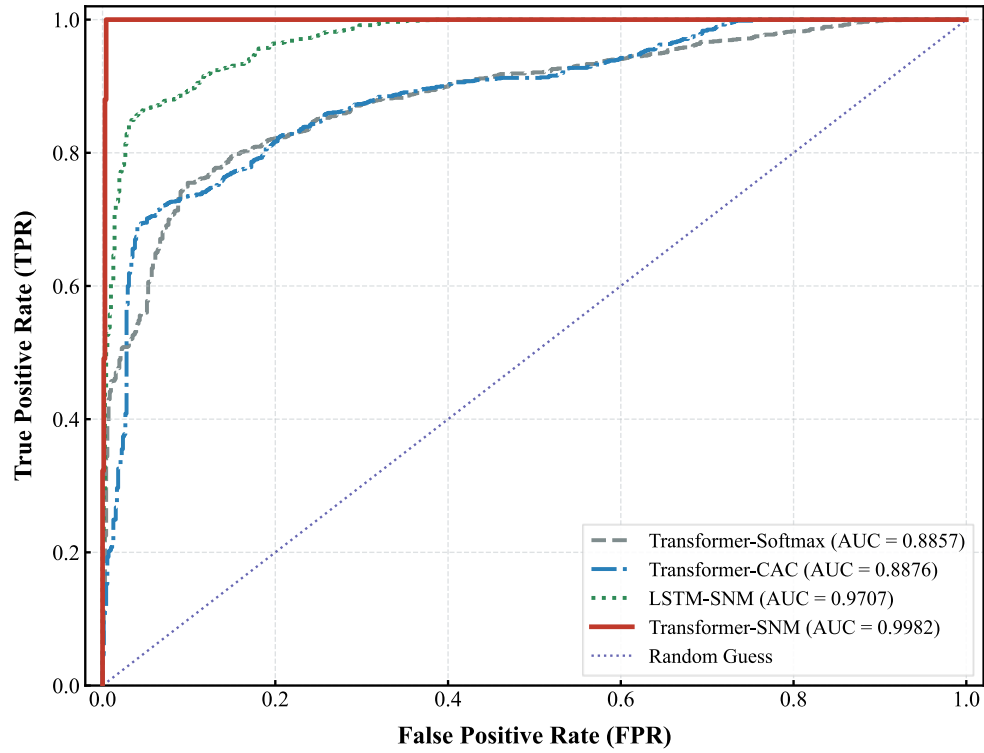


Figure 5. ROC curve comparison among multiple methods.

3.4 Multi-Position Robustness Analysis

The five positions in the Vergara dataset span distances of 1 to 4 meters from the gas release source, with signal intensity differences reaching several-fold to tens-fold. Figure 6 presents the performance of three methods across the five positions.

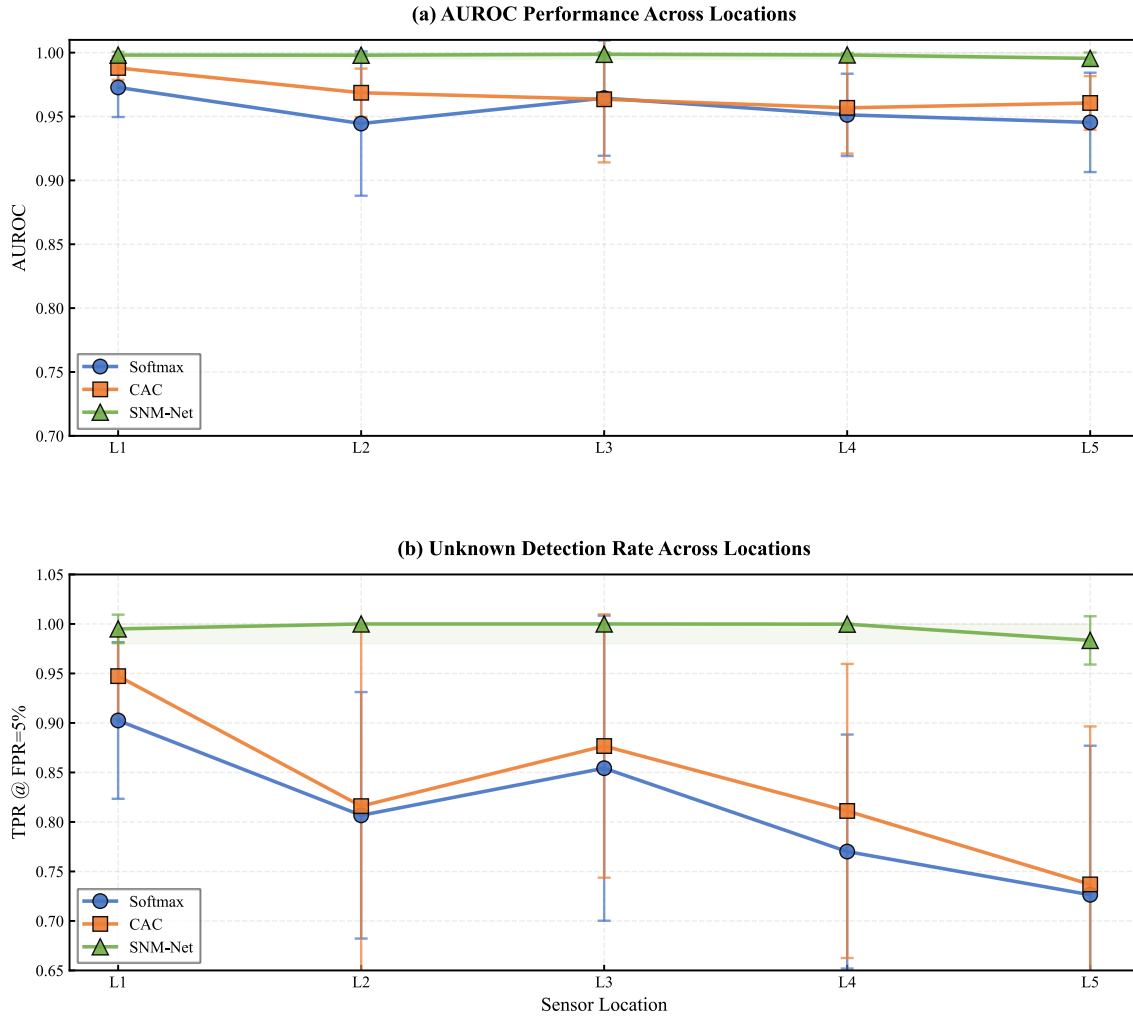


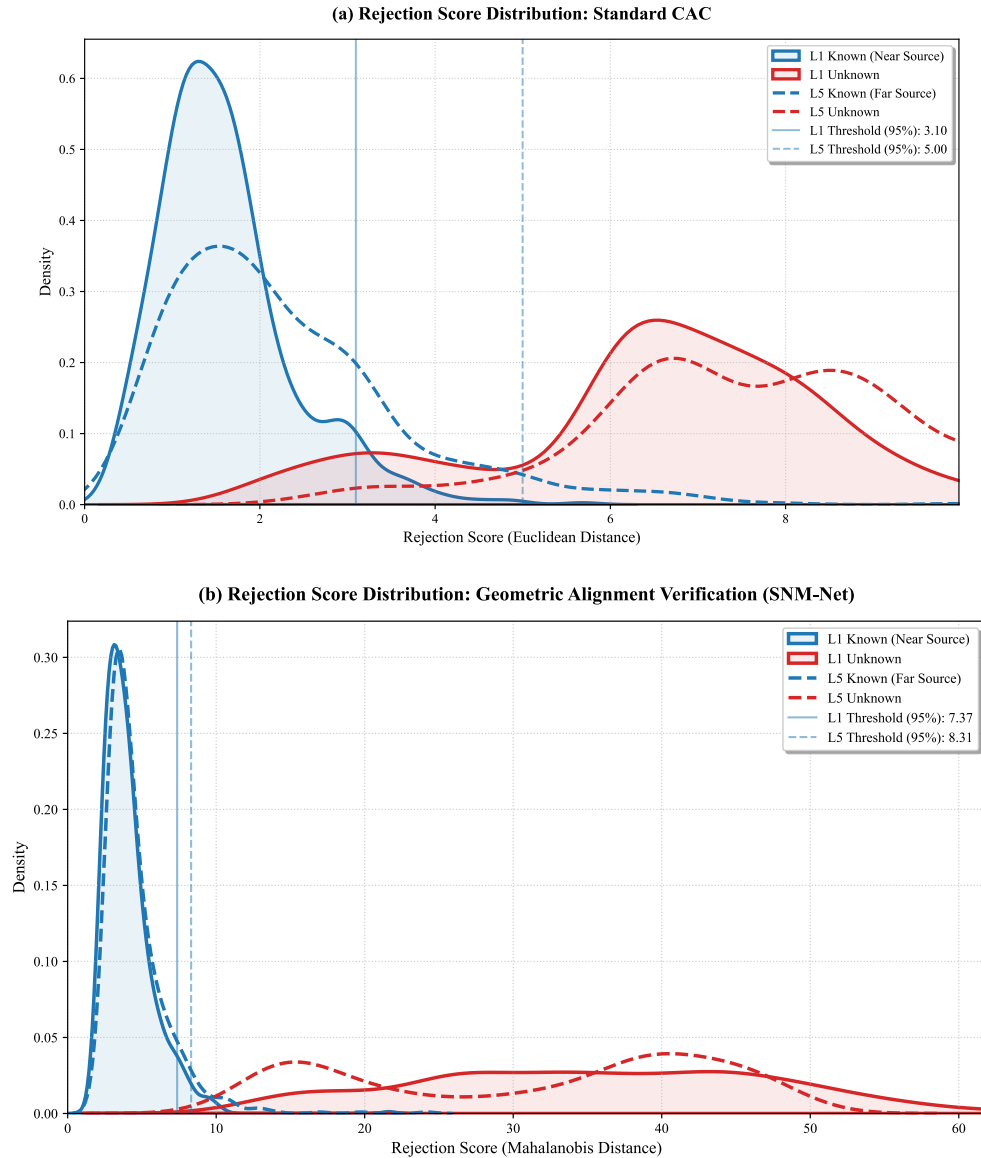
Figure 6. Multi-position robustness comparison charts. (a) AUROC performance (b) TPR@FPR=5%

SNM-Net achieves the following AUROC values across the five positions: L1=0.9982, L2=0.9990, L3=0.9989, L4=0.9965, and L5=0.9959. The standard deviation of AUROC across the five positions is merely 0.0013, indicating high model insensitivity to position variations. In contrast, the Softmax baseline exhibits a standard deviation of 0.0163, which is 12.5 times that of SNM-Net. Even at position L5 with the weakest signal, SNM-Net's TPR still reaches 98.34%, while CAC achieves only 73.69%. This position invariance stems from the spherical projection eliminating the influence of magnitude, enabling model decisions to rely solely on directional information.

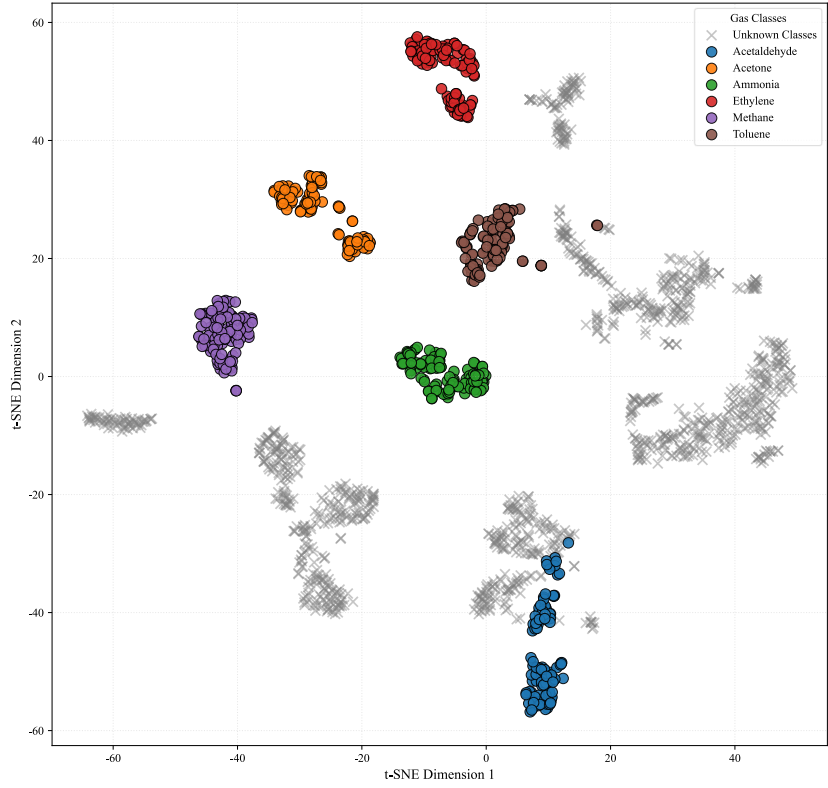
4. Discussion

4.1 Mechanistic Analysis

This section provides an in-depth analysis of the underlying mechanisms enabling SNM-Net's high performance through feature space visualization and decision space visualization. Figure 7 presents comparative visualization results between SNM-Net and the standard CAC method.



(c) t-SNE Feature Space Visualization: Standard CAC



(d) t-SNE Feature Space Visualization: SNM-Net

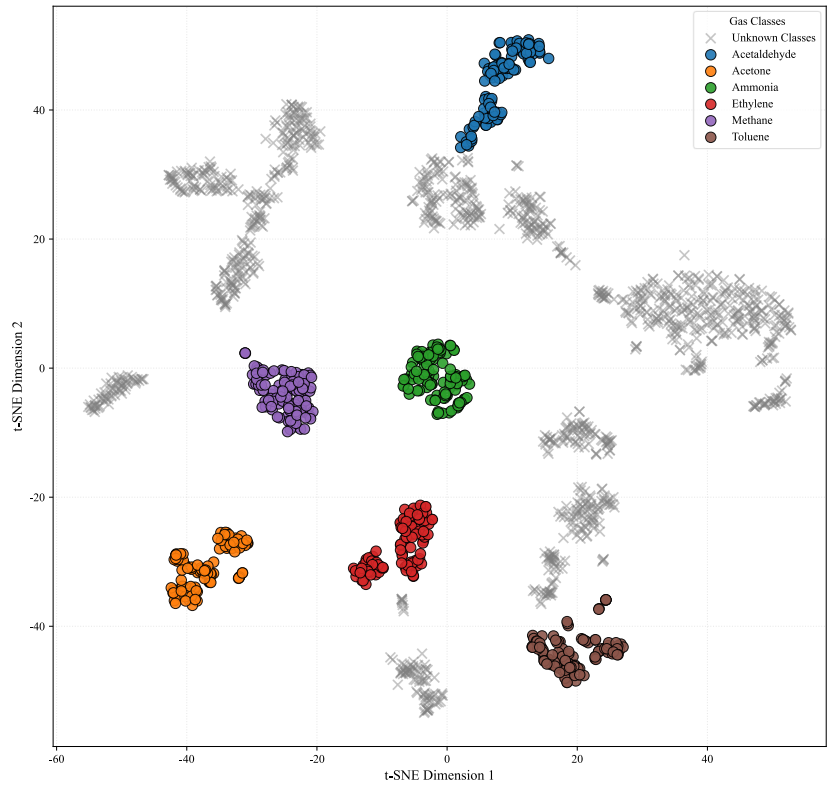


Figure 7. Visualization verification plots. (a) Rejection score distributions of standard CAC method at positions L1 and L5 (b) Rejection score distributions of SNM-Net at positions L1 and L5 (c) t-SNE feature space visualization of standard CAC method (d) t-SNE feature space visualization of SNM-Net

SNM-Net eliminates radial degrees of freedom at the physical level through spherical manifold projection, forcing the model to focus exclusively on directional vectors representing chemical properties. The core of this mechanism lies in the synergistic action of cascaded BN and L2N: batch normalization ensures input features possess stable distributions with zero mean and unit variance, providing consistent numerical conditions for L2 normalization; L2 normalization then projects all feature vectors onto the unit hypersphere, enabling model decisions to be based entirely on directional information, decoupled from signal intensity.

This mechanism is intuitively validated in the rejection score distributions. As shown in Figure 7(a), the rejection score distributions of known classes at positions L1 and L5 under the standard CAC method exhibit clear separation, with significant differences in 95th percentile thresholds. This position dependency implies that thresholds determined through training at one position may produce excessively high false positive rates or miss rates at other positions. In contrast, as shown in Figure 7(b), the known class distributions at positions L1 and L5 after SNM-Net processing exhibit high overlap, with 95th percentile threshold differences less than 0.02 units, demonstrating that the geometric refinement module successfully eliminates distribution drift caused by sensor position differences.

The fundamental advantage of Mahalanobis distance over Euclidean distance lies in its adaptivity to the geometric structure of feature distributions. Mahalanobis distance automatically learns anisotropic structures through covariance matrices: eigenvalues of the covariance matrix reflect variance magnitudes along principal component directions, while eigenvectors define the directions of principal components. Mahalanobis distance assigns higher weights to directions with small variance and lower weights to directions with large variance, resulting in ellipsoidal decision boundaries that adaptively conform to the true data manifold. The t-SNE visualization results (Figures 7c-d) demonstrate that SNM-Net significantly improves feature space structure: known classes form more

compact clusters, inter-class separation becomes clearer, and unknown class samples are effectively repelled to peripheral regions of the feature space.

The combination of spherical constraints and Mahalanobis distance forms a powerful synergistic effect. Spherical projection reduces the intrinsic dimensionality of features by eliminating radial degrees of freedom, making feature distributions more regular; Mahalanobis distance then precisely captures the covariance structure of directional features on the sphere, achieving adaptive decision boundaries. From a signal processing perspective: geometric normalization eliminates the primary source of drift (amplitude variations), while statistical scoring handles remaining feature distribution differences (covariance structure in the directional domain).

4.2 In-Depth Comparison with Existing Methods

EVM is based on extreme value theory, assuming that samples near class boundaries follow Weibull distributions. However, this method underperforms in this study, even slightly worse than the simple Softmax baseline. Analysis suggests that EVM's core assumptions may deviate from the actual characteristics of gas sensor data. Responses of gas-sensitive sensors are influenced by multiple physicochemical processes, and their feature distributions may exhibit atypical tail behaviors. Furthermore, EVM requires estimating boundary sample distributions in high-dimensional feature spaces, and relatively limited sample sizes may lead to inaccurate distribution estimation.

CAC effectively enhances intra-class feature compactness through the introduction of class anchor concepts and anchor constraint loss. However, CAC has two inherent limitations: it employs Euclidean distance as the scoring mechanism, which cannot adapt to anisotropic distributions of gas features; and it lacks dedicated drift handling mechanisms—when signal intensity changes, feature vector magnitudes change accordingly, causing Euclidean distance to produce deviations. SNM-Net simultaneously addresses both issues through geometric refinement and Mahalanobis distance.

4.3 Threshold Stability and Practical Value

Although this study employs adaptive thresholds in the experimental protocol to ensure fair comparison, the distribution overlap phenomenon in Figure 7(b) reveals an important finding: SNM-Net actually possesses the potential to use a globally fixed threshold. The core challenge faced by

traditional methods is that rejection score distributions differ significantly under different conditions, causing thresholds determined under one condition to fail under others. SNM-Net eliminates this condition dependency through geometric refinement, meaning a single global threshold can be used to adapt to all positions, significantly reducing system deployment complexity and maintenance costs.

The high TPR performance achieved by SNM-Net has direct practical value in multiple industrial scenarios. In industrial safety monitoring, high TPR means the system misses virtually no potential threats, reducing miss rates to below 0.43%. In food quality control, high TPR ensures that substandard products are reliably identified and eliminated. In environmental monitoring, high TPR guarantees that regulatory authorities can promptly detect and respond to novel pollution events. The fixed 5% false positive rate constraint ensures system practicality, and SNM-Net achieves a 99.57% detection rate under this constraint, achieving an optimal balance between precision and practicality.

4.4 Limitations and Future Work

The training and testing data in this study originate from the same sensor array device, and the model's transfer capability across different devices has not yet been validated. Due to manufacturing variations and different aging states among sensor batches, cross-device deployment may face additional domain shift challenges. Future work will explore the combination of domain adaptation techniques with SNM-Net to enhance cross-device generalization capability. Additionally, although theoretical analysis indicates that SNM-Net incurs low computational overhead, systematic latency and power consumption tests on actual embedded platforms have not yet been conducted.

5. Conclusion

This study addresses the core challenges of open-set gas recognition in E-nose systems through an innovative geometric perspective. SNM-Net achieves feature-intensity decoupling through spherical normalization and constructs adaptive ellipsoidal decision boundaries through Mahalanobis distance, demonstrating three key innovations: feature space geometric reconstruction that eliminates interference from signal intensity fluctuations at the physical root; a statistical scoring mechanism that captures anisotropic feature distributions through covariance modeling; and an architecture-agnostic design that seamlessly enhances various backbone networks.

Systematic experiments on the Vergara gas sensor dataset validate the framework's effectiveness. Ablation experiments clearly demonstrate the individual contributions of each component, while cross-architecture validation demonstrates universal applicability. Compared to state-of-the-art methods, SNM-Net achieves a 3.02 percentage point improvement in AUROC and a 91.0% reduction in standard deviation, maintaining exceptional robustness across all five sensor positions. SNM-Net's unknown detection rate reaches 99.57%, and this breakthrough performance enables practical industrial deployment. This work establishes a new performance benchmark for drift-robust open-set gas recognition and provides solid theoretical and technical support for reliable machine olfaction systems in real industrial environments.

References

- [1] W.S. Al-Dayyeni, S. Al-Yousif, M.M. Taher, A.W. Al-Faouri, N.M.D. Tahir, M.M. Jaber, F. Ghabban, I.A. Najm, I.M. Alfadli, O.Z. Ameerbakhsh, M.J. Mnati, N.A. Al-Shareefi, A.H. Saleh, A review on electronic nose: coherent taxonomy, classification, motivations, challenges, recommendations and datasets, *IEEE Access* 9 (2021) 88535–88551.
- [2] T.C. Pearce, S.S. Schiffman, H.T. Nagle, J.W. Gardner, *Handbook of Machine Olfaction: Electronic Nose Technology*, Wiley-VCH, Weinheim, 2003.
- [3] J. Fonollosa, B. Halford, L. Fonseca, J. Santander, S. Udina, M. Moreno, J. Hildenbrand, J. Wöllenstein, S. Marco, Ethylene optical spectrometer for apple ripening monitoring in controlled atmosphere store-houses, *Sens. Actuators B Chem.* 136 (2009) 546–554.
- [4] D. Compagnone, M. Faieta, D. Pizzoni, C. Di Natale, R. Paolesse, T. Van Caelenberg, B. Beheydt, P. Pittia, Quartz crystal microbalance gas sensor arrays for the quality control of chocolate, *Sens. Actuators B Chem.* 207 (2015) 1114–1120.
- [5] D.R. Wijaya, R. Sarno, E. Zulaika, DWTLSTM for electronic nose signal processing in beef quality monitoring, *Sens. Actuators B Chem.* 326 (2021) 128931.
- [6] S.Y. Kim, B.S. Kang, A colorimetric sensor array-based classification of coffees, *Sens. Actuators B Chem.* 275 (2018) 277–283.

[7] V.H. Tran, H.P. Chan, M. Thurston, P. Jackson, C. Lewis, D. Yates, G. Bell, P.S. Thomas, Breath analysis of lung cancer patients using an electronic nose detection system, *IEEE Sens. J.* 10 (2010) 1514–1518.

[8] D.F. Altomare, F. Porcelli, A. Picciariello, M. Pinto, M. Di Lena, O. Caputi Iambrenghi, I. Ugenti, A. Guglielmi, L. Vincenti, G. De Gennaro, The use of the PEN3 e-nose in the screening of colorectal cancer and polyps, *Tech. Coloproctol.* 20 (2016) 405–409.

[9] M. Tonezzer, D.T.T. Le, S. Iannotta, N. Van Hieu, Selective discrimination of hazardous gases using one single metal oxide resistive sensor, *Sens. Actuators B Chem.* 277 (2018) 121–128.

[10] J. Zhang, Y. Xue, Q. Sun, T. Zhang, Y. Chen, W. Yu, Y. Xiong, X. Wei, G. Yu, H. Wan, P. Wang, A miniaturized electronic nose with artificial neural network for anti-interference detection of mixed indoor hazardous gases, *Sens. Actuators B Chem.* 326 (2021) 128822.

[11] H. Li, D. Luo, Y. Sun, H. Gholamhosseini, Classification and identification of industrial gases based on electronic nose technology, *Sensors* 19 (2019) 5033.

[12] O. Hotel, J.P. Poli, C. Mer-Calfati, E. Scorsone, S. Saada, A review of algorithms for SAW sensors e-nose based volatile compound identification, *Sens. Actuators B Chem.* 255 (2018) 2472–2482.

[13] J. Yan, X. Guo, S. Duan, P. Jia, L. Wang, C. Peng, S. Zhang, Electronic nose feature extraction methods: a review, *Sensors* 15 (2015) 27804–27831.

[14] P. Peng, X. Zhao, X. Pan, W. Ye, Gas classification using deep convolutional neural networks, *Sensors* 18 (2018) 157.

[15] Y.J. Liu, Q.H. Meng, X.N. Zhang, Data processing for multiple electronic noses using sensor response visualization, *IEEE Sens. J.* 18 (2018) 9360–9369.

[16] D. Ma, J. Gao, Z. Zhang, H. Zhao, Gas recognition method based on the deep learning model of sensor array response map, *Sens. Actuators B Chem.* 330 (2021) 129349.

[17] J.C. Rodriguez Gamboa, A.J. da Silva, I.C. Ismael, E.S. Albarracin E, C.M. Duran A, Validation of the rapid detection approach for enhancing the electronic nose systems performance, using different deep learning models and support vector machines, *Sens. Actuators B Chem.* 327 (2021) 128921.

[18] J. Chu, W. Li, X. Yang, Y. Wu, D. Wang, A. Yang, H. Yuan, X. Wang, Y. Li, M. Rong, Identification of gas mixtures via sensor array combining with neural networks, *Sens. Actuators B Chem.* 329 (2021) 129090.

[19] S.H. Wang, T.I. Chou, S.W. Chiu, K.T. Tang, Using a hybrid deep neural network for gas classification, *IEEE Sens. J.* 21 (2021) 6401–6407.

[20] N. Imam, T.A. Cleland, Rapid online learning and robust recall in a neuromorphic olfactory circuit, *Nat. Mach. Intell.* 2 (2020) 181–191.

[21] L. Zhang, F. Tian, L. Dang, G. Li, X. Peng, X. Yin, S. Liu, A novel background interferences elimination method in electronic nose using pattern recognition, *Sens. Actuators A Phys.* 201 (2013) 254–263.

[22] L. Zhang, D. Zhang, Efficient solutions for discreteness, drift, and disturbance (3D) in electronic olfaction, *IEEE Trans. Syst. Man Cybern. Syst.* 48 (2018) 242–254.

[23] J. Tan, J. Xu, Applications of electronic nose (e-nose) and electronic tongue (e-tongue) in food quality-related properties determination: A review, *Artif. Intell. Agric.* 4 (2020) 104–115.

[24] C. Geng, S. Huang, S. Chen, Recent advances in open set recognition: A survey, *IEEE Trans. Pattern Anal. Mach. Intell.* 43 (2021) 3614–3631.

[25] L. Neal, M. Olson, X. Fern, W.K. Wong, F. Li, Open set learning with counterfactual images, in: *Proc. European Conference on Computer Vision*, Springer, 2018, pp. 620–635.

[26] W.J. Scheirer, A. de Rezende Rocha, A. Sapkota, T.E. Boult, Toward open set recognition, *IEEE Trans. Pattern Anal. Mach. Intell.* 35 (2013) 1757–1772.

[27] A. Bendale, T.E. Boult, Towards open set deep networks, in: *Proc. IEEE Conf. Comput. Vis. Pattern Recognit.*, 2016, pp. 1563–1572.

[28] E.M. Rudd, L.P. Jain, W.J. Scheirer, T.E. Boult, The extreme value machine, *IEEE Trans. Pattern Anal. Mach. Intell.* 40 (2018) 762–768.

[29] D. Miller, N. Sunderhauf, M. Milford, F. Dayoub, Class anchor clustering: A loss for distance-based open set recognition, in: *Proc. IEEE Winter Conf. Appl. Comput. Vis.*, 2021, pp. 3570–3578.

[30] C. Qu, C. Liu, Y. Gu, S. Chai, C. Feng, B. Chen, Open-set gas recognition: A case-study based on an electronic nose dataset, *Sens. Actuators B Chem.* 360 (2022) 131652.

[31] Ma, X., Wu, F., Yue, J., Feng, P., Peng, X., & Chu, J. (2024). MSE-TCN: Multi-scale temporal convolutional network with channel attention for open-set gas classification. *Microchemical Journal*, 207, 111814.

[32] A. Vergara, J. Fonollosa, J. Mahiques, M. Trincavelli, N. Rulkov, R. Huerta, On the performance of gas sensor arrays in open sampling systems using Inhibitory Support Vector Machines, *Sens. Actuators B Chem.* 185 (2013) 462–477.

[33] M.K. Muezzinoglu, A. Vergara, R. Huerta, N. Rulkov, M.I. Rabinovich, A. Selverston, H.D.I. Abarbanel, Acceleration of chemo-sensory information processing using transient features, *Sens. Actuators B Chem.* 137 (2009) 507–512.

[34] A. Vergara, E. Llobet, J. Brezmes, P. Ivanov, C. Cané, I. Gràcia, X. Vilanova, X. Correig, Quantitative gas mixture analysis using temperature-modulated micro-hotplate gas sensors: Selection and validation of the optimal modulating frequencies, *Sens. Actuators B Chem.* 123 (2007) 1002–1016.

[35] A. Vergara, S. Vembu, T. Ayhan, M.A. Ryan, M.L. Homer, R. Huerta, Chemical gas sensor drift compensation using classifier ensembles, *Sens. Actuators B Chem.* 166–167 (2012) 320–329.

[36] S. De Vito, E. Massera, M. Piga, L. Martinotto, G. Di Francia, On field calibration of an electronic nose for benzene estimation in an urban pollution monitoring scenario, *Sens. Actuators B Chem.* 129 (2008) 750–757.

[37] T. Artursson, T. Eklöv, I. Lundström, P. Mårtensson, M. Sjöström, M. Holmberg, Drift correction for gas sensors using multivariate methods, *J. Chemom.* 14 (2000) 711–723.

- [38] L. Zhang, D. Zhang, Domain adaptation extreme learning machines for drift compensation in E-nose systems, *IEEE Trans. Instrum. Meas.* 64 (2015) 1790–1801.
- [39] R. Yi, J. Yan, D. Shi, Y. Tian, F. Chen, Z. Wang, Improving the performance of drifted/shifted electronic nose systems by cross-domain transfer using common transfer samples, *Sens. Actuators B Chem.* 329 (2021) 129162.
- [40] Q. Liu, X. Hu, M. Ye, X. Cheng, F. Li, Gas recognition under sensor drift by using deep learning, *Int. J. Intell. Syst.* 30 (2015) 907–922.
- [41] Z. Liang, F. Tian, C. Zhang, H. Sun, A. Song, T. Liu, A correlated information removing based interference suppression technique in electronic nose for detection of bacteria, *Anal. Chim. Acta* 986 (2017) 145–152.
- [42] K. Yan, D. Zhang, Correcting instrumental variation and time-varying drift: A transfer learning approach with autoencoders, *IEEE Trans. Instrum. Meas.* 65 (2016) 2012–2022.
- [43] R. Yoshihashi, W. Shao, R. Kawakami, S. You, M. Iida, T. Naemura, Classification-reconstruction learning for open-set recognition, in: *Proc. IEEE Conf. Comput. Vis. Pattern Recognit.*, 2019, pp. 4011–4020.
- [44] M. Gunther, S. Cruz, E.M. Rudd, T.E. Boulton, Toward open-set face recognition, in: *Proc. IEEE Conf. Comput. Vis. Pattern Recognit. Workshops*, 2017, pp. 573–582.